A Combined Modeling and Experimental Study of Tensile Properties of Additively Manufactured Polymeric Composite Materials

Lingbin Meng[1], Xuehui Yang[1], Eduardo Salcedo[1], Dong-Cheon Baek[2], Jong Eun Ryu[3*], Zhe Lu[4], Jing Zhang[1**]

1. Department of Mechanical and Energy Engineering, Indiana University-Purdue University Indianapolis, IN 46202, USA
2. Reliability Assessment Center, Korea Institute of Machinery and Materials, 171 Jang-dong, Yuseong-gu, Daejeon 34103, Republic of Korea
3. Department of Mechanical and Aerospace Engineering, North Carolina State University, Raleigh, NC 27695, USA
4. School of Materials and Metallurgical Engineering, University of Science and Technology of Liaoning, China

Corresponding author: *jryu@ncsu.edu 919-515-5265; **jz29@iupui.edu; 317-278-7186

Abstract

In this study, the mechanical properties, in terms of stress-strain curves, of additively manufactured polymeric composite materials, Tango Black Plus (TB+), Vero White Plus (VW+), and their intermediate materials with different mixing ratios, are reported. The ultimate tensile strength and elongation at break are experimentally measured using ASTM standard tensile test. As the content of VM+ increases, the strength of the polymeric materials increases and elongation decreases. Additionally, the Shore A hardness of the materials increases with reduced TB+ concentration. In parallel to the experiment, hyperelastic models are employed to fit the experimental stress-strain curves. The shear modulus of the materials is obtained from the Arruda-Boyce model, and it increases with reduced concentration of TB+. Due to the good quality of the fitted data, it is suggested that the Arruda-Boyce model is the best model for modeling the additively manufactured polymeric materials. With the well characterized and modeled mechanical properties of these hyperelastic materials, designers can conduct computational study for application in flexible electronics field.

Keywords: Additive manufacturing; hyperelastic model; mechanical property; polymeric material

---

This is the author's manuscript of the article published in final edited form as:

Meng, L., Yang, X., Salcedo, E., Baek, D.-C., Ryu, J. E., Lu, Z., & Zhang, J. (2020). A Combined Modeling and Experimental Study of Tensile Properties of Additively Manufactured Polymeric Composite Materials. Journal of Materials Engineering and Performance, 29(4), 2597–2604. https://doi.org/10.1007/s11665-020-04746-5

1.Introduction

Additive manufacturing (AM) is a layer-upon-layer fabrication processes and previously applied for rapid prototyping. In the last decade, AM technology has evolved into a decent alternative for direct fabrication of tools and functional parts. One of the favorable features of AM technology is to 3D print polymeric materials for flexible electronics [1]. Currently, among various AM processes, material jetting is the one that possesses the capability of combining multiple polymeric materials and varying material compositions or type within the layers [2, 3], which can improve part performance by adding more complexity and functionality (e.g. functionally graded materials [4]). In a typical material jetting process, the inkjet head moves in the x and y-axes depositing one or multiple photopolymers which are then smoothed by a roller and cured by ultraviolet light after each layer is finished [5].

In contrast to conventional subtractive manufacturing processes, the properties of AM materials are affected by many manufacturing factors, which make these properties different from conventional materials. Several previous studies have examined the factors affecting material properties. For example, due to the layer-upon-layer nature, orientation effect on the properties of material jetting materials has been investigated [6-9]. In addition, material properties are also affected by aging and storage conditions [7, 9], as well as warm-up time and cleanliness of nozzles [9]. This process-structure-property relationship for material jetting process has been reviewed by Ref. [10].

Accurate description of the mechanical properties is essential for subsequent design and applications of the AM materials. This becomes more critical for polymeric materials since they experience much larger deformations compared to metals. Selected mechanical properties of common polymers fabricated by material jetting technique are provided by the manufacturer [11]. However, there is no complete description of the mechanical property, especially in the form of stress-strain curve. Additionally, discrepancy exists among the reported data [6, 7]. In this regard, acquiring accurate mechanical properties by reliable experimental measurement and using physical models to describe the material behaviors are strongly desirable for designers. These are also the objectives of this work.

Forerunners have put forward many hyperelastic models for polymeric materials to better

describe their tensile behaviors. These hyperelastic models can be further divided into two groups: (1) phenomenological models, such as Neo-Hookean Model [12], Mooney-Rivlin Model [12, 13], Ogden Model [14], Yeoh Model [15], and Gent model [16], and (2) constitutive models, such as Arruda-Boyce model [17] and Tehrani-Sarvestani model [18], which provide physical connections between the model parameters and mechanical properties of materials. Recently, some applications of phenomenological models for additively manufactured hyperelastic polymeric materials have been reported [4, 19, 20]. However, due to lack of physical meaning, the outcomes of these applications are merely some meaningless model parameters which can only be used to reconstruct the stress-strain curves. A constitutive model with meaningful parameters will be preferred for designers. To this end, selected constitutive models will be used in this study.

This work focuses on two popular types of polymeric materials for flexible electronics fabricated by the material jetting technique, Tango Black Plus (TB+) and Vero White Plus (VW+). The tensile properties of them and their composites are systematically studied using a combined experimental and modeling approach. More specifically, the objectives of this work are addressed by the following three steps: (1) the stress-strain curves of the polymeric materials are experimentally measured using ASTM standard tensile tests. Hardness measurement and microstructure analysis are also conducted; (2) some selected hyperelastic models are briefly reviewed and employed to model the stress-strain response; (3) the models are evaluated based on the fitting performance and the physical meaning of the fitted parameters. The outcome of this work is twofold: (1) The well modeled tensile behaviors and reliable mechanical properties of the polymeric materials will be helpful for designers to conduct computational design and simulation such as finite element analysis, and (2) the hyperelastic models with good fitting performance and physical meaning will be recommended for future study of similar polymeric materials for flexible electronics.

2. Methodology

2.1 Experimental details

Two Polyjet polymeric materials, a rubber-like material, Tango Black Plus (TB+), and a

rigid opaque material, Vero White Plus (VW+), and their mixtures with different mixing ratios are investigated: TB+, DM40, DM50, DM60, DM70, DM85, DM95, and VW+. The numbers after each material abbreviation "DM" represent its Shore A hardness provided by the manufacturer [11].

The tensile test specimens were printed using a PolyJet printer (Connex 500, Stratasys Ltd.), which has the multi-material jetting capacity and can achieve uniform mixing of multiple materials. The ASTM D638 standard is followed. To ensure high accuracy, the layer thickness was set to be 30 μm, and standard support setting. Two samples of each material were fabricated in the preset concentrations.

The uniaxial tensile test was conducted under the ambient condition at 20 °C. The tester used is a universal testing machine (Instron 5567) with a contact strain gauge. During the test, the grip keeps moving at a constant speed of 50 mm/min until break.

2.2 Hyperelastic models of polymeric materials

Hyperelastic models describe the stress-strain response in terms of strain energy, W. The principal Cauchy stress is related to the partial derivative of strain energy:

$$\sigma_i = \lambda_i \frac{\partial W}{\partial \lambda_i} + p \ \ (i = 1, 2, 3), \tag{1}$$

where p is an arbitrary pressure and λ_i is the principal values of the stretch, such that

$$\lambda_i = 1 + \varepsilon_i^{\mathrm{Eng}} \ \ (i = 1, 2, 3). \tag{2}$$

To eliminate the arbitrary pressure, the stress-stretch relations are frequently written in the form of difference in two principal stresses:

$$\sigma_1 - \sigma_2 = \lambda_1 \frac{\partial W}{\partial \lambda_1} - \lambda_2 \frac{\partial W}{\partial \lambda_2}. \tag{3}$$

To include the Poisson's effect into Eqs. (1) and (3), stretch invariants I_1, I_2 and I_3 have to be taken into account. The expressions of the three invariants are

$$I_1 = \lambda_1^2 + \lambda_2^2 + \lambda_3^2; \tag{4a}$$

$$I_2 = \lambda_1^2\lambda_2^2 + \lambda_2^2\lambda_3^2 + \lambda_1^2\lambda_3^2; \tag{4b}$$

$$I_3 = \lambda_1^2\lambda_2^2\lambda_3^2. \tag{4c}$$

Therefore, hyperelastic models can describe strain energy W in terms of I_1 and I_2.

Rubber-like materials are usually assumed to be fully incompressible. Under this premise, $I_3 = 1$, which means

$$\lambda_1\lambda_2\lambda_3 = 1; \tag{5}$$

$$I_2 = \frac{1}{\lambda_1^2} + \frac{1}{\lambda_2^2} + \frac{1}{\lambda_3^2}. \tag{6}$$

For an incompressible material, according to Eqs. (3-6), after some substitutions and arrangements, the following equation can be derived:

$$\sigma_1 - \sigma_2 = 2(\lambda_1^2 - \lambda_2^2)\left(\frac{\partial W}{\partial I_1} + \lambda_3^2\frac{\partial W}{\partial I_2}\right). \tag{7}$$

2.2.1 Arruda-Boyce model

The Arruda-Boyce model is the first complete constitutive model proposed by Arruda and Boyce in 1993. This model is based on the statistical mechanics of a material with a cubic representative volume element containing eight chains along the diagonal directions [17]. Before the Arruda-Boyce model, this concept with three chains [21] or four chains [22] was put forward but their simulated results were highly dependent upon the state of imposed deformation [17]. Materials in the Arruda-Boyce model are usually assumed to be incompressible.

For chains in the Arruda-Boyce model, the fully extended length is given by $r_L = lN$ where N is the number of statistical links of length l, and the initial chain length $r_0 = \sqrt{N}l$ is taken from a random walk consideration of N steps of l [17]. An important parameter in Arruda-Boyce model, limiting network stretch, or locking stretch, λ_L, is then given by

$$\lambda_L = \frac{r_L}{r_0} = \sqrt{N}. \tag{8}$$

The Arruda-Boyce model expresses the strain energy W in terms of the first stretch invariant I_1, and use of inverse Langevin function. A reasonable approximation of Arruda-Boyce model is taking the first five terms of the inverse Langevin function, such that [17]

$$W = G\sum_{i=1}^{5}\alpha_i\lambda_L^{2-2i}\left(I_1^i - 3^i\right), \tag{9}$$

where $\alpha_1 = \frac{1}{2}$, $\alpha_2 = \frac{1}{20}$, $\alpha_3 = \frac{11}{1050}$, $\alpha_4 = \frac{19}{7000}$, $\alpha_5 = \frac{519}{673750}$, and $G = n\kappa\Theta$ is a material constant, in which n is the chain density, κ is the Boltzmann constant, and Θ is the absolute

temperature.

Another parameter involved in Arruda-Boyce model is the shear modulus, μ, which is related to G. In an undeformed condition, the following equation has to be satisfied:

$$\left.\frac{\partial W}{\partial I_1}\right|_{I_1=3} = \frac{\mu}{2}. \tag{10}$$

According to Eqs. (9) and (10), the following equation can then be derived:

$$\mu = G\left(1 + \frac{3}{5\lambda_L^2} + \frac{99}{175\lambda_L^4} + \frac{513}{875\lambda_L^6} + \frac{42039}{67375\lambda_L^8}\right). \tag{11}$$

Under uniaxial tensile stress, $\sigma_2 = \sigma_3 = 0$, and if the materials are assumed to be isotropic, then $\lambda_2 = \lambda_3$. According to Eq. (5),

$$\lambda_2 = \lambda_3 = \frac{1}{\sqrt{\lambda_1}}. \tag{12}$$

According to Eq. (7) and (12), after some substitutions and arrangements,

$$\sigma_1 = 2G\left(\lambda_1^2 - \frac{1}{\lambda_1}\right)\sum_{i=1}^{5} i\alpha_i \lambda_L^{2-2i} I_1^{i-1}. \tag{13}$$

Therefore, the engineering stress is

$$\sigma_1^{\text{Eng}} = \frac{\sigma_1}{\lambda_1} = 2G\left(\lambda_1 - \frac{1}{\lambda_1^2}\right)\sum_{i=1}^{5} i\alpha_i \lambda_L^{2-2i} I_1^{i-1}. \tag{14}$$

Once the two parameters in Arruda-Boyce model are obtained, the fitted stress-strain curve of the material can then be plotted using Eqs. (2), (11) and (14).

2.2.2 Mooney-Rivlin model

The Mooney-Rivlin model expresses the strain energy W in terms of I_1 and I_2. In the Mooney-Rivlin model, the strain energy is given by [12, 13]

$$W = \sum_i \sum_j C_{ij}(I_1 - 3)^i (I_2 - 3)^j + D(J-1)^2, \tag{15}$$

where $J = \sqrt{I_3} = \lambda_1\lambda_2\lambda_3$. If a material is fully incompressible, then $J = 1$. D is a constant describing the incompressibility of the material and can be eliminated if the material is assumed to be fully incompressible. The constants C_{ij} and D will be determined by curve-fitting.

In Eq. (15), if both i and j are taken from the range of 0 to 1, then 3 parameters, C_{01}, C_{10}, and C_{11}, will be determined by curve-fitting and used to describe the curve. If the range is 0 to 2, then 5 parameters will be involved. Materials can always be perfectly fitted by more parameters of Mooney-Rivlin models. However, due to lack of physical meaning, the Mooney-

Rivlin model should be used with caution.

Under uniaxial tensile stress, with the same deriving process in the Arruda-Boyce model, the engineering stress in the 5-parameter Mooney-Rivlin model is

$$\sigma_1^{\mathrm{Eng}} = 2\left(\lambda_1 - \frac{1}{\lambda_1^2}\right)\left[C_{10} + C_{11}\left(2\lambda_1 + \frac{1}{\lambda_1^2} - 3\right) + 2C_{20}\left(\lambda_1^2 + \frac{2}{\lambda_1} - 3\right)\right] + 2\left(1 - \frac{1}{\lambda_1^3}\right)\left[C_{01} + C_{11}\left(\lambda_1^2 + \frac{2}{\lambda_1} - 3\right) + 2C_{02}\left(2\lambda_1 + \frac{1}{\lambda_1^2} - 3\right)\right]. \quad (16)$$

2.2.3 Neo-Hookean and Gent hyperelastic models

The Neo-Hookean model is an inchoate phenomenological model and has been superseded by Mooney-Rivlin model. The Neo-Hookean model does not predict that increase in modulus at large strains and is typically accurate only for strains less than 20% [23]. The strain energy of the Neo-Hookean model is given by

$$W = \frac{1}{2}G(I_1 - 3) + D(J - 1)^2. \quad (17)$$

It is worth mentioning that when the limit network stretch of the Arruda-Boyce model, λ_L, is sufficiently large, or when the deformation is sufficiently small, the Arruda-Boyce model will reduce to the Neo-Hookean model. The former proposition can be easily derived by eliminating the terms with λ_L in the denominator in Eq. (9). In addition, the Neo-Hookean model is also a special case of the Mooney-Rivlin model when only one parameter, C_{10}, is taken into account.

The Gent model is a phenomenological model based on the concept of limiting network stretch, λ_L. It has been shown in Ref. [24] that the Gent model is a simplified approximation of the Arruda–Boyce model. In this study, the Neo-Hookean model and Gent hyperelastic model were evaluated, but the results are not presented in this paper.

2.2.4 Modeling tensile test using the hyperelastic models to 3D printed polymeric materials

The stress-strain curves acquired from the tensile tests in Section 2.1 are imported to the material library in ANSYS for analysis. The fitting algorithms in ANSYS are employed to fit the experimental data and compute the model parameters. The fitted stress-strain curves are retrieved using Eq. (14) and Eq. (16) and compared with experimental data. Since Arruda-

Boyce model is a constitute model, it is preferential if its fitted curve matches the experimental data.

3. Results and discussion

3.1 Experimental results

3.1.1 Stress-strain curves

The experimental stress-strain curves of all samples are summarized in Fig. 1. Since the two samples of each material show similar stress-strain curve, for each material only one stress-strain curve is displayed. These curves will be fitted by the hyperelastic models later. Because the magnitude of ultimate tensile strength of VW+ is much larger than others, its stress-strain curve is embedded as inset in Fig. 1. As shown in Fig. 1, as the content of rubber-like TB+ decreases, the 3D printed polymeric materials become harder, as demonstrated with increased stress and reduced strain. For DM95, since the concentration of TB+ in DM95 is too small, it possesses an obvious hardening region like a rigid material. The initial slopes in the stress-strain curves are the indication of Young's modulus. It is clear that the Young's modulus values increase with the increased concentration of VW+, the hard phase in the composite.

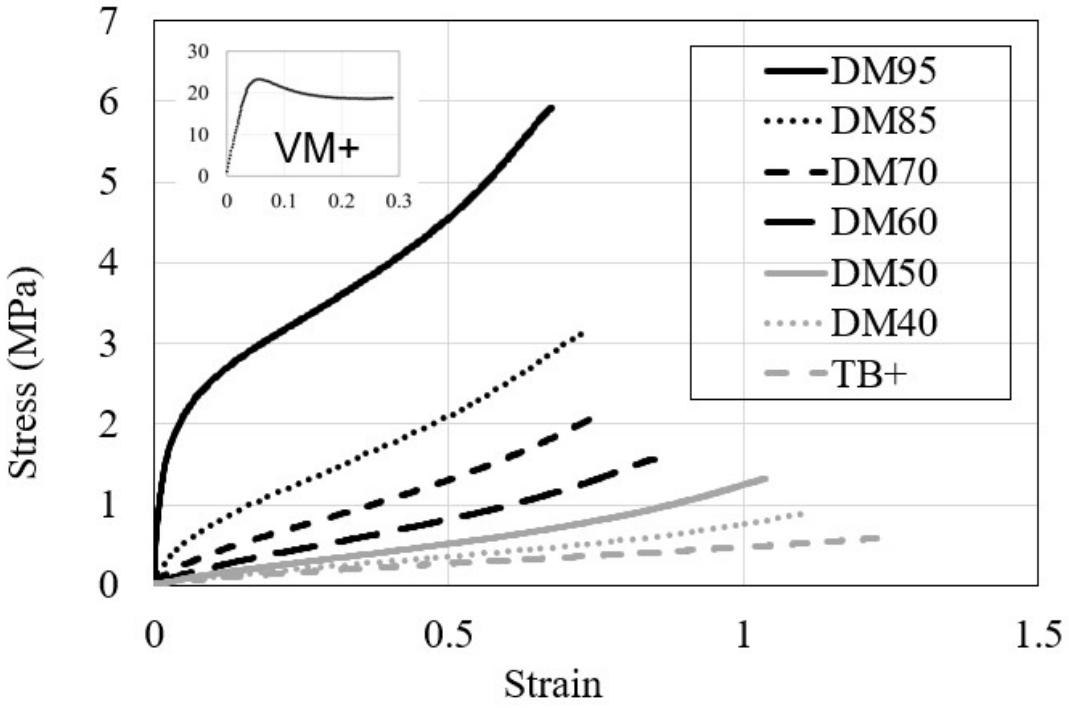

Figure 1: Experimental stress-strain curves of all samples, with VW+ as the inset.

Table 1 summarizes the experimentally measured ultimate tensile strength (σ_u) and elongation strain at break (ε_f). The data provided by the manufacturer [11] and Ref. [7] are also included in the table for comparison.

Table 1: Experimentally measured ultimate tensile strength σ_u and elongation strain at break ε_f in this study, compared with the literature data in Refs. [7] and [11]

	σ_u (MPa)			ε_f (%)		
	This study	Ref. [11]	Ref. [7]	This study	Ref. [11]	Ref. [7]
TB+	0.59	0.8-1.5	0.39	125	170-220	180
DM40	0.89	1.3-1.8	-	110	110-130	-
DM50	1.32	1.9-3.0	-	104	95-110	-
DM60	1.57	2.5-4.0	1.13	85	75-85	127
DM70	2.16	3.5-5.0	-	77	65-80	-
DM85	3.4	5.0-7.0	2.59	74	55-65	114

DM95	5.91	8.5-10.0	-	68	35-45	-
VW+	23.2	50-65	45.27	30	10-25	19

As shown in Table 1, the ultimate tensile strength values in this study are much lower than those provided by the manufacturer [11], but close to those of Ref. [7]. Regarding the elongation strain at break, the measured values are in good agreement with the manufacturer data [11], while lower than those of Ref. [7]. Please note that Refs. [7] and [11] only provide these properties, but not the full stress-strain curves, which are needed for accurately description of the large deformation in whole strain range. It should also be noted that the experimental settings to obtain the mechanical properties are not provided in Ref. [11], which means the data from Ref. [11] may not be reliable.

A potential reason causing the difference in the property data is the type of the extensometer. The experiment in this study uses a contact gauge, which works by exerting a load on the samples. In general, this load is not statistically significant. However, since the ultimate strength of the materials in this study is relatively low, this load may cause a difference compared to the results using a non-contact gauge. Another testing parameter, strain rate, may also contribute to deviation [25]. In addition, the aforementioned manufacturing factors may be also a reason. Different settings and orientations in printing procedure may cause large difference in the mechanical properties of samples. Optimization of the manufacturing factors for additively manufactured parts has been addressed by the applications of machine learning models in literature [26-29], which is beyond the scope of this work.

Fig. 2 shows the ultimate tensile strength and elongation at break of all samples, using the data in Table 1. As expected, it's clear that with increased concentration of VW+, ultimate tensile strength increases and elongation at break decreases. Similarly, the shear modulus is expected to have the same trend as ultimate tensile strength, as discussed later in the modeling results in Section 3.2.

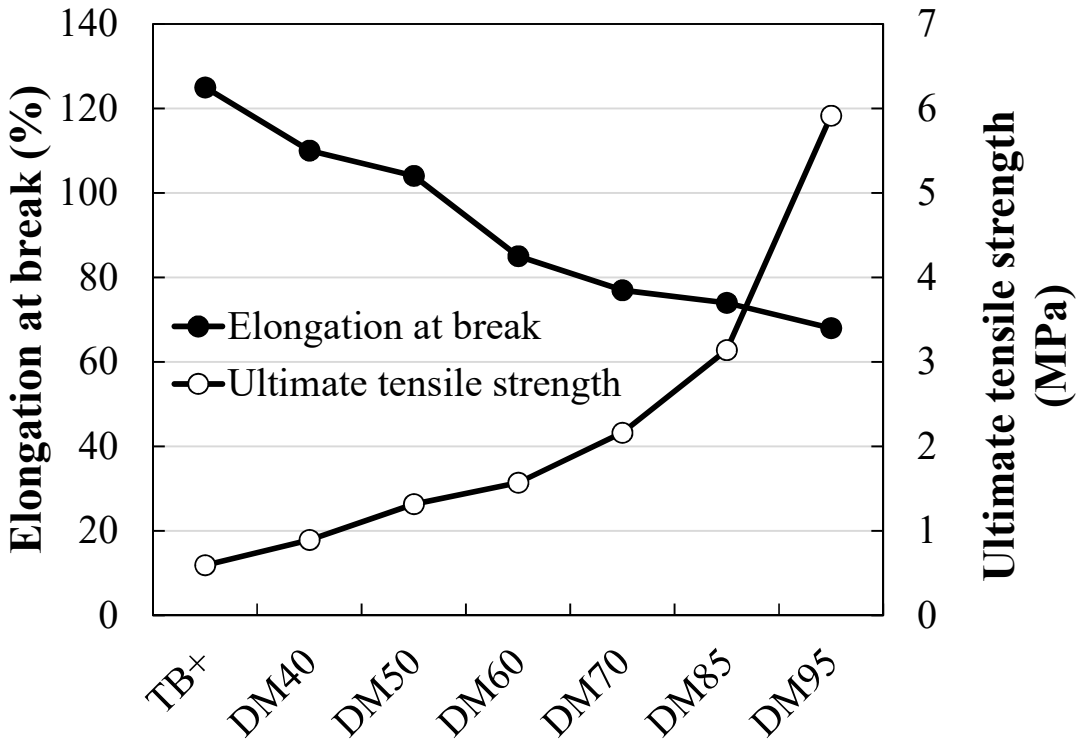

Figure 2: Ultimate tensile strength and elongation at break values of all printed materials except VW+.

3.1.2 Hardness and its correlation to ultimate strength and elongation at fracture

Since all materials in this study vary only in the concentration of VW+ and TB+, it is expected that there should be a trend in properties. In this study, due to lack of manufacturing information of exact concentration in these intermediate materials, the trend will be shown in terms of the sample name. As shown in Fig. 3, the Shore A hardness increases with reduced concentration of TB+. This is because TB+ is the soft phase in the composites.

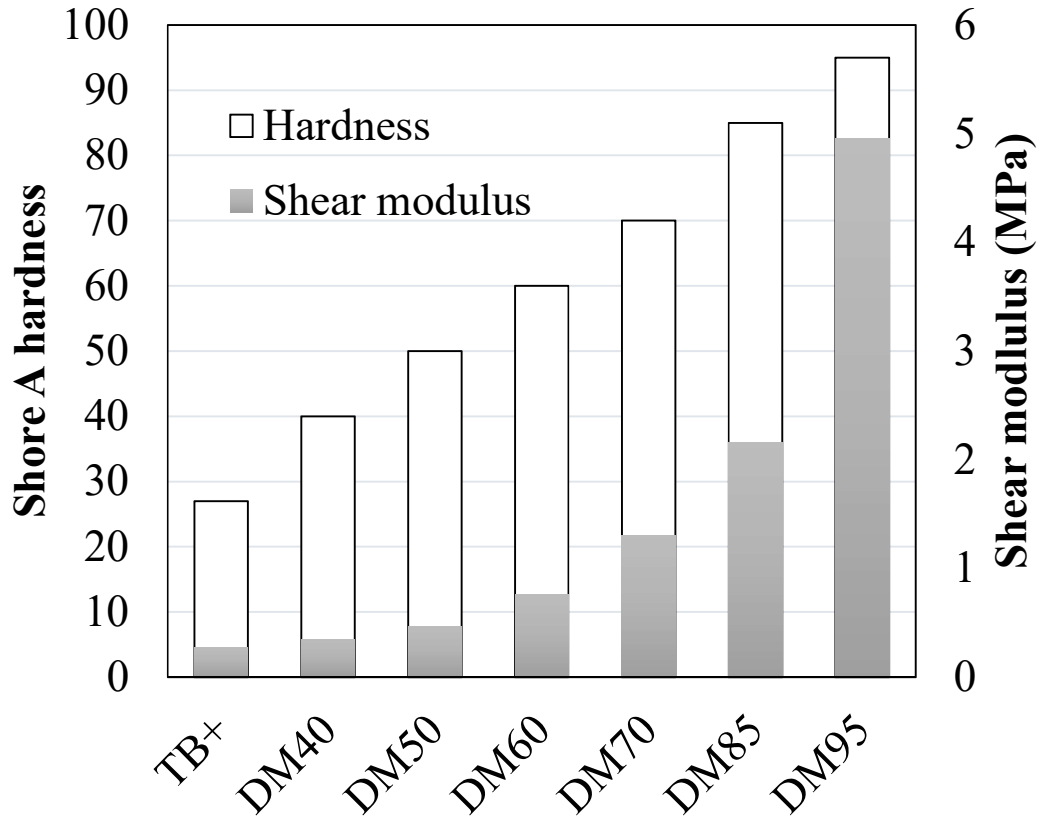

Figure 3: Measured Shore A hardness and simulated shear modulus of all samples except VW+.

3.1.3 Microstructure analysis

The optical images of fractured samples except VW+, after the tensile test are shown in Fig. 4. The samples recovered the elastic deformation after fracture, which indicates that they are indeed hyperelastic.

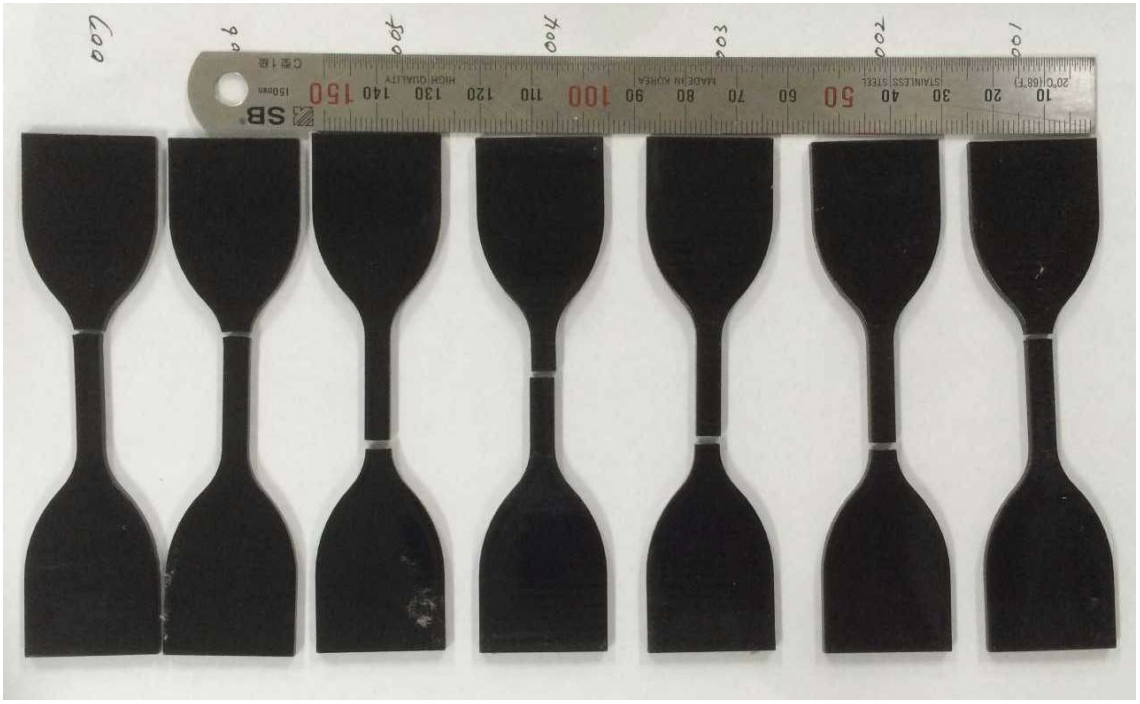

Figure 4: Optical images of the fractured samples (from left to right: DM95, DM85, DM70, DM60, DM50, DM40, TB+, except VW+).

The SEM images of the cross-section views of the fracture surfaces are shown in Fig. 5. As shown in the figure, as the content of TB+ is decreased, the fracture surfaces gradually change from ductile to brittle manner. Fig. 5a shows the fracture surface of TB+, whose flaky patterns are the indication of large elastic deformation and fracture tear in rubber materials. Figs. 5b - 5g show the fracture surfaces with wavy shape, suggesting a less ductile deformation manner. Fig. 5h shows a flat fracture surface, as expected in the brittle VW+ material. The SEM microstructure images are consistent to the observed stress-strain curve trend in Fig. 1.

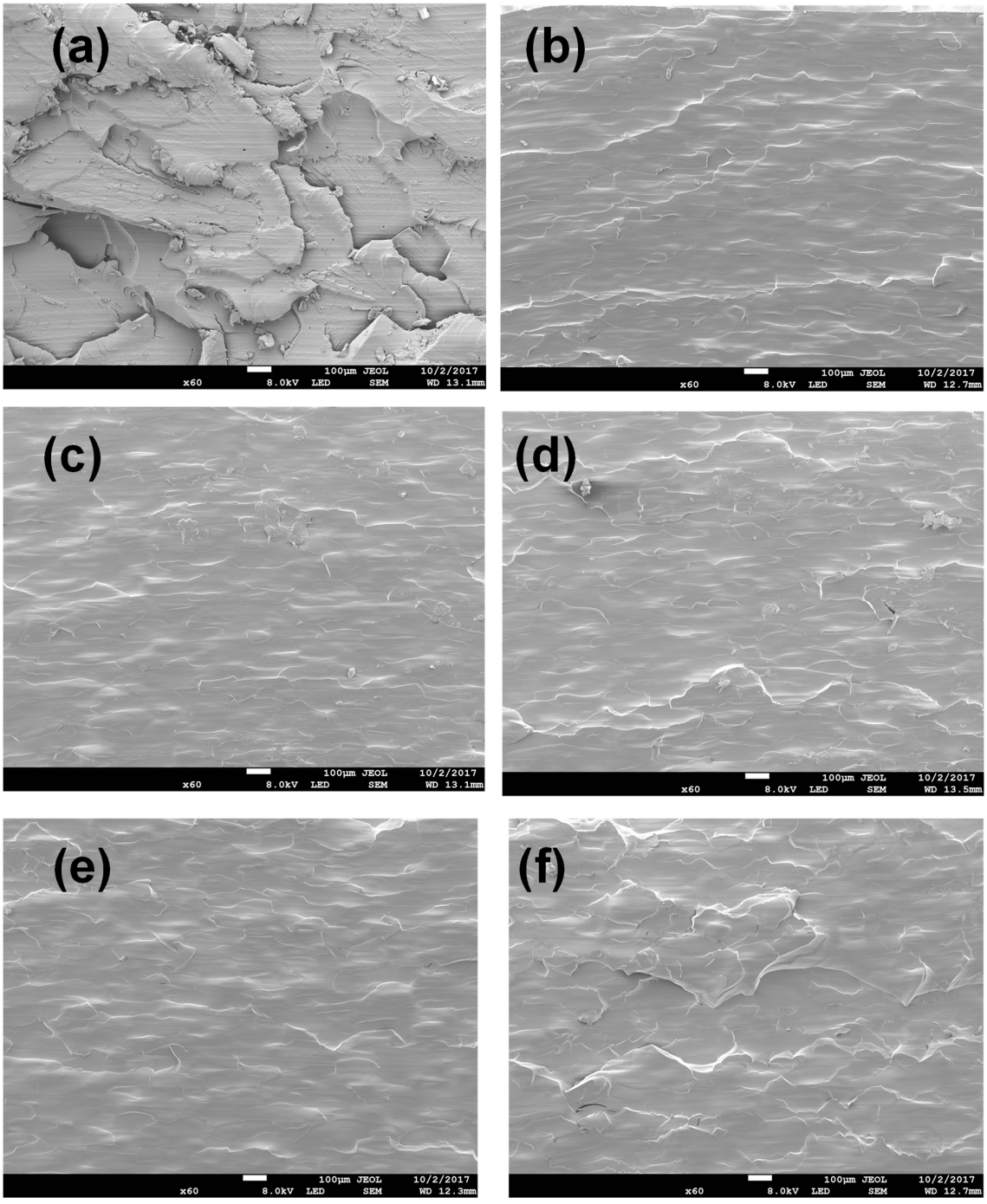
(a)
100µm JEOL 10/2/2017
x60 8.0kV LED SEM WD 13.1mm
(b)
100µm JEOL 10/2/2017
x60 8.0kV LED SEM WD 12.7mm
(c)
100µm JEOL 10/2/2017
x60 8.0kV LED SEM WD 13.1mm
(d)
100µm JEOL 10/2/2017
x60 8.0kV LED SEM WD 13.5mm
(e)
100µm JEOL 10/2/2017
x60 8.0kV LED SEM WD 12.3mm
(f)
100µm JEOL 10/2/2017
x60 8.0kV LED SEM WD 12.7mm

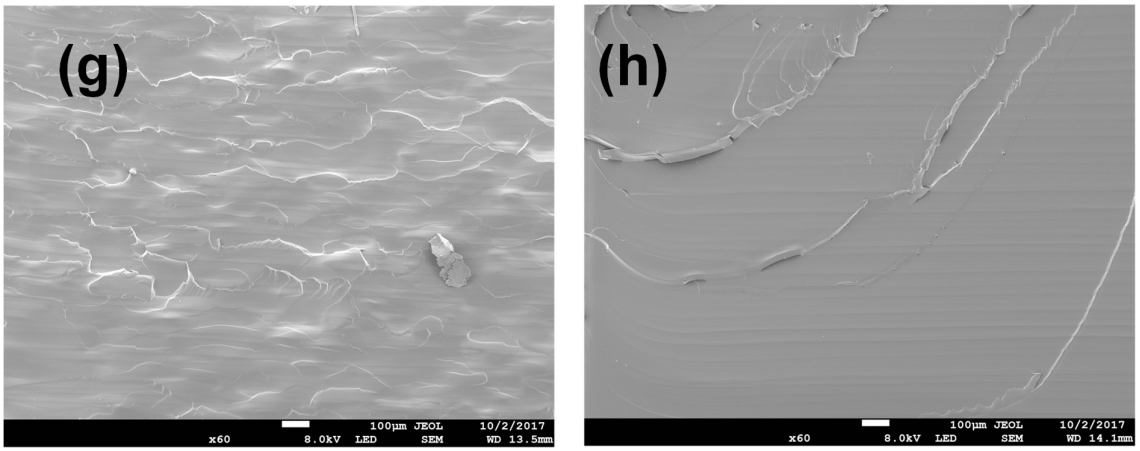

Figure 5: The SEM images of the cross-section views of the fracture surfaces. (a) TB+, (b) DM40, (c) DM50, (d) DM60, (e) DM70, (f) DM85, (g) DM95, and (h) VW+. The scale bar in the figure is 100 μm.

3.2 Hyperelastic modeling results

The stress-strain curves in Section 3.1 are fitted to Arruda-Boyce model using the fitting algorithms in the ANSYS material library. The retrieved stress-strain curves using the fitted parameters of all samples are shown in Fig. 6, compared against experimental curves. It is not necessary to perform the hyperelastic simulation to VW+ since it is a rigid material. From Fig. 6, it can be seen that for TB+ and DM40, DM50, DM60, DM70, and DM85, the Arruda-Boyce model successfully fits the experimental curves with good agreement.

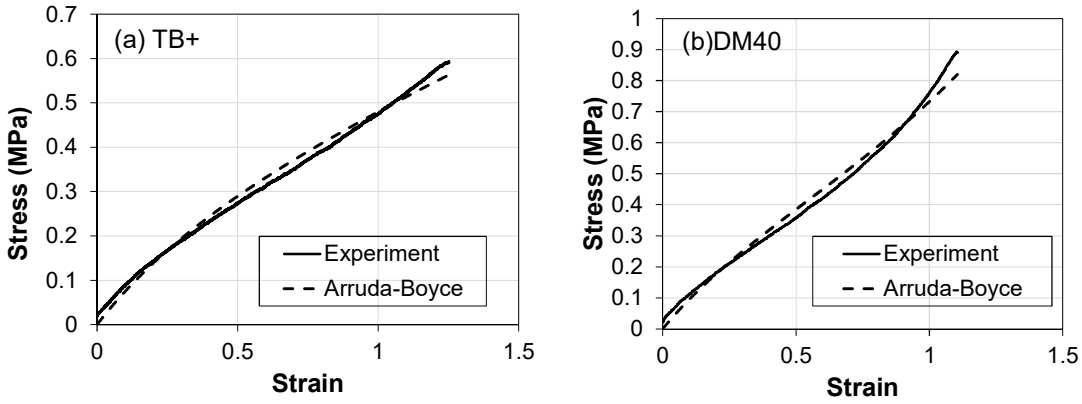

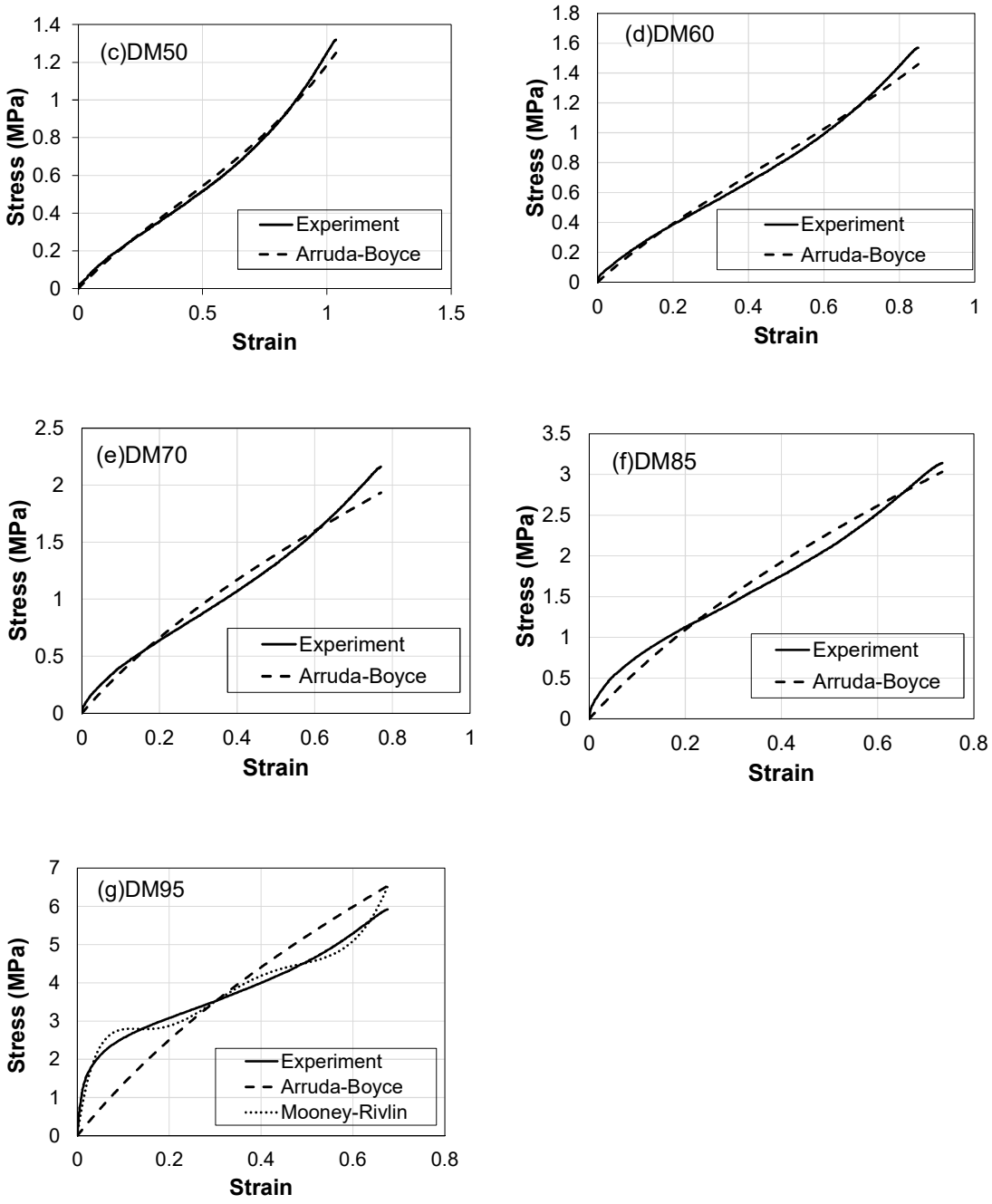

Figure 6: Simulated stress-strain curves using the Arruda-Boyce model, compared against experimental curves for (a) TB+, (b) DM40, (c) DM50, (d) DM60, (e) DM70, (f) DM85, and (g) DM95. The Mooney-Rivlin model is also included for comparison in (g) DM95.

Table 2 shows the performance of the hyperelastic models in terms of the root-mean-

squared error (RMSE) normalized by the ultimate tensile strength. The RMSE, normalized by the maximum value (i.e. ultimate tensile strength) in the dataset, can be used to quantitatively assess the model performance and directly compare with each other without considering the magnitude of different series of data. The normalized RMSE of Arruda-Boyce model for TB+, DM40, DM50, DM60, DM70 and DM85 is less then 0.05, indicating the excellent performance of Arruda-Boyce model. The verification of the performance of the Arruda-Boyce model for TB+, DM40, DM50, DM60, DM70 and DM85 also confirms the reliability of its outcomes (i.e. the shear modulus in Table 3). For DM95, large deviation between the fitted curve of Arruda-Boyce model and experimental curve is shown by both the visulization in Fig. 6(g) and the large value of normalized RMSE. This is reasonable, as hyperelastic models are designed to describe the tensile behaviors for hyperelastic materials, while DM95 shows an obvious hardening region and behaves more like a rigid material. In this case, the 5-parameter Mooney-Rivlin model is also employed for comparison. Note the material is assumed to be fully incompressible in the Mooney-Rivlin model. For DM95, the fitted parameters in the 5-paramenter Mooney-Rivlin model are (unit: MPa): C10 = -133.408, C01 =147.161, C20=145.6603, C11 = -466.481, and C02= 432.4102. The value of its normalized RMSE, 0.0304, indicates the good fitting performance of the 5-parameter Mooney-Rivlin model. If needed, an even better fitted curve can be obtained by simply increasing the number of parameters in the Mooney-Rivlin model. However, there is no physical meaning in these parameters.

Table 2: Root-mean-squared error (RMSE) normalized by the ultimate tensile stregnth

Material	Normalized RMSE (MPa)	
	Arruda-Boyce model	Mooney-Rivlin model
TB+	0.0253	\
DM40	0.0299	\
DM50	0.0205	\
DM60	0.0279	\
DM70	0.0404	\

DM85	0.0389	\
DM95	0.1254	0.0304

Table 3 shows the parameters derived from fitting the experimental curves using the Arruda-Boyce model - the limiting network stretch λ_L and shear modulus μ. The calculated shear modulus, μ, is included in Fig. 2. Note that the shear modulus of DM95 may not be accurate since the Arruda-Boyce model failed to fit it. In spite of this, it's clear that the shear modulus increases with increased concentration of VW+, which is the expected result.

Table 3: Derived material parameters used in the Arruda-Boyce model

Material	λ_L	μ (MPa)
TB+	1.89×10^{7}	0.27418
DM40	1.9116	0.34675
DM50	1.5433	0.46799
DM60	1.6866	0.76580
DM70	3.8079	1.30639
DM85	4.74×10^{7}	2.16190
DM95	4.03×10^{8}	4.95370

Overall, the mechanical properties of two additively manufactured polymeric materials, VW+ and TB+, as well as their composite, are measured by experiments, and modeled by hyperelastic models. The well characterized and modeled mechanical behaviors of these hyperelastic materials enable designers to conduct computational study for applications in flexible electronics field. Based on the modeling results presented above, the Arruda-Boyce model works well for most flexible materials, except for DM95 who behaves more like a rigid material. Therefore, as a constitutive model, the Arruda-Boyce model is recommended for future design and optimization of additively manufactured hyperelastic materials.

4. Conclusions

In this paper, two additively manufactured polymeric materials, VW+ and TB+, along with their intermediate materials with different mixing ratios of the two materials are investigated by combined experiment and modeling studies. The conclusions are summarized as follows:

1. The ultimate tensile strength and elongation at break are experimentally determined from the tensile stress-strain curves. As the content of VM+ increases, the strength increases and the elongation decreases.

2. The cross-section views of the fracture surfaces reveal that, as the content of TB+ is decreased, the fracture surfaces gradually change from ductile to brittle manner, which is consistent to the observed trend in the experimental stress-strain curves.

3. The Shore A hardness of the materials increases with reduced concentration of TB+.

4. The shear modulus of each flexible material is obtained by fitting the Arruda-Boyce model, and it increases with reduced concentration of TB+.

5. Due to the good quality of the fitted data, it is suggested that the Arruda-Boyce model is the best model for future design and optimization of additively manufactured hyperelastic materials.

Acknowledgments

LM and JZ acknowledge the support provided by"Human Resources Program in Energy Technology (No. 20194030202450)", "Power Generation & Electricity Delivery grant (No. 20193310100030)" of the Korea Institute of Energy Technology Evaluation and Planning (KETEP). ZL acknowledges the financial support provided by the National Natural Science Foundation of China (No. 51702145), and innovation group project from the University of Science and Technology Liaoning (2017TD01). JR was supported by the Department of Mechanical and Aerospace Engineering at NCSU. JR would also like to acknowledge the Integrated Nanosystems Development Institute (INDI) for use of their FESEM, which was

awarded through the NSF grant MRI-1229514. DCB was supported by the Technology Innovation Program (or Industrial Strategic Technology Development Program(10078310, Development of High Speed Multi-pass DTP System) funded by the Ministry of Trade, Industry & Energy(MOTIE), Korea.

References

1. Yin, Z., et al., *Inkjet printing for flexible electronics: Materials, processes and equipments.* Chinese Science Bulletin, 2010. **55**(30): p. 3383-3407.
2. ASTM, *ASTM F2792-12a: Standard Terminology for Additive Manufacturing Technologies*. 2012, ASTM International: West Conshohocken, PA.
3. Vaezi, M., et al., *Multiple material additive manufacturing–Part 1: a review: this review paper covers a decade of research on multiple material additive manufacturing technologies which can produce complex geometry parts with different materials.* Virtual and Physical Prototyping, 2013. **8**(1): p. 19-50.
4. Salcedo, E., et al., *Simulation and validation of three dimension functionally graded materials by material jetting.* Additive Manufacturing, 2018. **22**: p. 351-359.
5. Wong, K.V. and A. Hernandez, *A review of additive manufacturing.* ISRN Mechanical Engineering, 2012. **2012**.
6. Barclift, M.W. and C.B. Williams. *Examining variability in the mechanical properties of parts manufactured via polyjet direct 3D printing*. in *International Solid Freeform Fabrication Symposium*. 2012.
7. Bass, L., N.A. Meisel, and C.B. Williams, *Exploring variability of orientation and aging effects in material properties of multi-material jetting parts.* Rapid Prototyping Journal, 2016. **22**(5): p. 826-834.
8. Blanco, D., P. Fernandez, and A. Noriega, *Nonisotropic experimental characterization of the relaxation modulus for PolyJet manufactured parts.* Journal of Materials Research, 2014. **29**(17): p. 1876-1882.
9. Mueller, J., K. Shea, and C. Daraio, *Mechanical properties of parts fabricated with inkjet 3D printing through efficient experimental design.* Materials & Design, 2015. **86**: p. 902-912.
10. Kim, H., Y. Lin, and T.-L.B. Tseng, *A review on quality control in additive manufacturing.* Rapid Prototyping Journal, 2018. **24**(3): p. 645-669.
11. StratasysLtd. *Digital Materials Data Sheet*. 2014; Available from: http://www.stratasys.com/materials/polyjet/digital-materials.
12. Rivlin, R.S., *Large elastic deformations of isotropic materials.* Philosophical Transactions of the Royal Society of London. Series A, Mathematical and Physical Sciences, 1948. **241**(835): p. 379-397.
13. Mooney, M., *A theory of large elastic deformation.* Journal of Applied Physics, 1940. **11**(9): p. 582-592.
14. Ogden, R.W., *Large deformation isotropic elasticity – on the correlation of theory and experiment for incompressible rubberlike solids.* Proceedings of the Royal Society of London. Series A, Mathematical and Physical Sciences, 1972. **326**(1567): p. 565-584.
15. Yeoh, O.H., *Some forms of the strain energy function for rubber.* Rubber Chemistry and technology, 1993. **66**(5): p. 754-771.
16. Gent, A.N., *A new constitutive relation for rubber.* Rubber Chemistry and Technology, 1996. **69**: p. 59-61.
17. Arruda, E.M. and M.C. Boyce, *A three-dimensional model for the large stretch behavior of rubber elastic materials.* Journal of the Mechanics and Physics of Solids,

1993. **41**(2): p. 389-412.
18. Tehrani, M. and A. Sarvestani, *Effect of chain length distribution on mechanical behavior of polymeric networks.* European Polymer Journal, 2017. **87**: p. 136-146.
19. Ryu, J.E., et al., *Material models and finite analysis of additively printed polymer composites.* Journal of Composite Materials, 2019. **53**(3): p. 361-371.
20. Morris, K., et al., *Uniaxial and biaxial testing of 3D printed hyperelastic photopolymers.* Journal of Applied Polymer Science, 2019: p. 48400.
21. Wang, M.C. and E. Guth, *Statistical Theory of Networks of Non-Gaussian Flexible Chains.* The Journal of Chemical Physics, 1952. **20**(7): p. 1144-1157.
22. Flory, P.J. and J.J. Rehner, *Statistical Mechanics of Cross-Linked Polymer Networks I. Rubberlike Elasticity.* The Journal of Chemical Physics, 1943. **11**(11): p. 512-520.
23. Gent, A.N., *Engineering with Rubber*. 2001, Munich: Carl Hanser Verlag.
24. Horgan, C.O. and G. Saccomandi, *Phenomenological Hyperelastic Strain-Stiffening Constitutive Models for Rubber.* Rubber Chemistry and Technology, 2006. **79**(1): p. 152-169.
25. Hutchinson, J. and K. Neale, *Influence of strain-rate sensitivity on necking under uniaxial tension.* Acta Metallurgica, 1977. **25**(8): p. 839-846.
26. Meng, L. and J. Zhang, *Process Design of Laser Powder Bed Fusion of Stainless Steel Using a Gaussian Process-Based Machine Learning Model.* JOM, 2019: p. 1-9.
27. Tapia, G., A. Elwany, and H. Sang, *Prediction of porosity in metal-based additive manufacturing using spatial Gaussian process models.* Additive Manufacturing, 2016. **12**: p. 282-290.
28. Tapia, G., et al., *Gaussian process-based surrogate modeling framework for process planning in laser powder-bed fusion additive manufacturing of 316L stainless steel.* The International Journal of Advanced Manufacturing Technology, 2018. **94**(9-12): p. 3591-3603.
29. Zhang, J., P. Wang, and R.X. Gao, *Deep learning-based tensile strength prediction in fused deposition modeling.* Computers in Industry, 2019. **107**: p. 11-21.